HAL
open science

Ureasil-polyether-CoFe 2 O 4 nanocomposites: Coupling drug delivery system and magnetic hyperthermia

Willian Max O. S. de Santana, Sébastien Abramson, Rodolfo Fini, Bruno L Caetano, Christine Ménager, Sandra H Pulcinelli, Celso V Santilli

▶ To cite this version:

Willian Max O. S. de Santana, Sébastien Abramson, Rodolfo Fini, Bruno L Caetano, Christine Ménager, et al.. Ureasil-polyether-CoFe 2 O 4 nanocomposites: Coupling drug delivery system and magnetic hyperthermia. ACS Applied Polymer Materials, 2021, 3 (10), pp.4837-4848. 10.1021/acsapm.1c00496 . hal-03525734

HAL Id: hal-03525734

https://hal.sorbonne-universite.fr/hal-03525734v1

Submitted on 14 Jan 2022

HAL is a multi-disciplinary open access archive for the deposit and dissemination of scientific research documents, whether they are published or not. The documents may come from teaching and research institutions in France or abroad, or from public or private research centers.

L'archive ouverte pluridisciplinaire **HAL**, est destinée au dépôt et à la diffusion de documents scientifiques de niveau recherche, publiés ou non, émanant des établissements d'enseignement et de recherche français ou étrangers, des laboratoires publics ou privés.

Ureasil-polyether-$CoFe_2O_4$ nanocomposites: Coupling drug delivery system and magnetic hyperthermia

*Willian Max O. S. de Santana [a], Sébastien Abramson [b], Rodolfo Fini [a], Bruno L. Caetano [a,b,c], Christine Ménager [b], Sandra H. Pulcinelli [a] and Celso V. Santilli [a] **

[a] Institute of Chemistry, São Paulo State University (UNESP), Araraquara, São Paulo, 14800-900, Brazil

[b] Physico-chimie des Electrolytes et Nanosystèmes Interfaciaux, PHENIX, Sorbonne Université, CNRS, F-75005 Paris, France

[c] Soft Matter Sciences and Engineering, ESPCI Paris, PSL University, Sorbonne Université, CNRS, F-75005 Paris, France

***Corresponding author.** E-mail addresses: cv.santilli@unesp.br;

KEYWORDS: Organic-inorganic hybrid materials, siloxane-polyether, nanocomposites, cobalt ferrite, magnetic hyperthermia.

ABSTRACT: In this work, we evaluate the effect of the ureasil-polyether hybrid nature on the magnetic hyperthermia (MH) properties of nanocomposites prepared by the conjugation of cobalt ferrite ($CoFe_2O_4$) superparamagnetic nanoparticles (SPN) with ureasil-poly(propylene oxide) (UPPO) and ureasil-poly(ethylene oxide) (UPEO). The results of small-angle X-ray scattering (SAXS) and differential scanning calorimetry (DSC) analyses evidenced that the nanoscopic structure and thermal properties remained essentially unaffected by conjugation of the SPN with the hybrid material. The UPPO-$CoFe_2O_4$ nanocomposite promoted higher efficiency of MH compared to the UPEO-$CoFe_2O_4$ nanocomposite, which was attributed to the difference in heat capacity of these composites. The temperature variations achieved by UPPO-$CoFe_2O_4$ and UPEO-$CoFe_2O_4$ were 34 and 20 ºC, respectively, when subjected to an alternating magnetic field (AMF) for 240 s. The drug delivery patterns of sodium diclofenac (SDCF) from UPPO and UPEO were unaffected by the conjugation with SPN or by MH.

1. INTRODUCTION

Magnetic hyperthermia (MH) is a safe way to raise the temperature of anatomical regions (to ~42-46 ºC), using the heat generated by superparamagnetic nanoparticles (SPN) when exposed to an alternating magnetic field (AMF).[1,2] For SPN, the conversion of magnetic energy into heat can be attributed to two different phenomena: (i) Néel relaxation, where energy dissipation occurs by rearrangement of the magnetic dipole moments inside the crystal, when the particle orientation remains fixed; (ii) Brownian relaxation, where heat is released by the rotation of the particle, with

the magnetic moments remaining fixed along the axis of the crystal.[1,3,4] MH has been consolidated as an anticancer therapy, used alone or combined with conventional therapies such as chemotherapy and radiotherapy.[1,5] In such biomedical applications, maghemite (γ-Fe_2O_3) and magnetite (Fe_3O_4) SPN are most commonly used, although recent research has highlighted the enhanced magnetic properties and the greater MH efficiency of cobalt ferrite ($CoFe_2O_4$).[6,7]

SPN has been associated with polymeric materials in the forms of microgels, injectable and topical hydrogels, and solid adhesives, for the design of nanocomposites with applications in tissue engineering, drug administration, and cancer treatments.[8,9] In these materials, the SPN can be incorporated by methods including mixing with a polymer precursor solution, precipitation reaction inside a polymeric matrix, or by grafting with polymer chains, where the functionalized SPN acts as nano-crosslinkers.[8] Despite the improved mechanical, thermal, and chemical stabilities of organic-inorganic hybrids (OIH), compared to three-dimensional networks consisting of purely organic or inorganic polymers, OIH have still been little explored in the design of SPN nanocomposites.[9,10]

The OIH of the ureasil-polyether family, such as ureasil-poly(ethylene oxide) (UPEO) and ureasil-poly(propylene oxide) (UPPO), are based on a siloxane framework covalently connected to polyether chains by urea bridges (−NH (C═O) NH−).[11,12] These hybrids can be prepared in the forms of films, gels, and hydrogels, offering attractive features as drug delivery systems, including:[13] (i) the ability to host high loadings of medications;[14,15] (ii) transparency, flexibility, insolubility in aqueous media, and thermal stability;[12,16] (iii) biocompatibility, good skin adhesion, and excellent film-forming ability;[15,17–19] (iv) hydrogel behavior (swelling) that can be tuned by controlling the hybrid matrix composition[19,20] or by using clay nanoparticles as diffusion barriers.[21] Unlike UPEO, the UPPO hybrids present low water uptake due to the hydrophobicity of the PPO

macromer, which can restrict drug release from the hybrid matrix.[12,15] Therefore, since the drug release profiles of ureasil-polyether hybrids are usually related to the swelling capacities of these materials, UPPO hybrids are more appropriate for the sustained release of low doses of drugs.[12,15,22]

In research exploring the relevance and potential applications of drug delivery systems coupled with MH, investigating the characteristics of ureasil-polyether hybrids, we recently reported the development of γ-Fe_2O_3 SPN/UPEO nanocomposites with the dual functionality of drug delivery and MH.[23] Most studies of SPN/polymer nanocomposites have been dedicated to understanding how the efficiencies of these materials for MH are influenced by the characteristics of the SPN, such as size, state of aggregation, and concentration.[24–26] In this work, we show the influence of the UPPO and UPEO hybrid matrices on the MH effect of nanocomposites containing $CoFe_2O_4$ SPN. These nanocomposites were prepared from the PEO and PPO with a molar weight of 1900 e 400 g mol^{-1}, respectively (PEO1900 and PPO400 macromers) using the sol-gel route and were loaded with sodium diclofenac (SDCF) as a model drug. The selection of these two polymers was based on the fact that the thermal behavior of the hybrid materials without SPN (UPEO1900 and UPPO400) are distinct at room temperature since UPPO hybrids are amorphous, while UPEO hybrids are semicrystalline. In this way, it was possible to evaluate the influence of the crystallinity of the hybrid matrix on the thermal and MH behaviors of the UPEO-CoFe and UPPO-CoFe nanocomposites. The morphological, nanostructural, and thermal characteristics of the hybrid nanocomposites, as well as their hyperthermia effects and drug release capacities, were evaluated by techniques including Fourier transform infrared spectroscopy (FTIR), differential scanning calorimetry (DSC), small-angle X-ray scattering (SAXS), UV-Vis spectrometry, and MH measurements.

2. EXPERIMENTAL SECTION

2.1 Materials

Cobalt(II) nitrate hexahydrate ($Co(NO_3)_2.6H_2O$, 98%, CAS no. 10026-22-9), iron(III) chloride hexahydrate ($FeCl_3.6H_2O$, CAS no. 10025-77-1), sodium hydroxide (NaOH, CAS no. 1310-73-2), iron(III) nitrate nonahydrate ($Fe(NO_3)_3.9H_2O$, CAS no. 7782-61-8), nitric acid (HNO_3, 70%, CAS no. 7697-37-2), O,O′-bis(2-aminopropyl)polypropylene glycol-block-polyethylene glycol-block-polypropylene glycol with molar weight of 1900 $g{\cdot}mol^{-1}$ (PEO1900, CAS no. 65605-36-9), O,O′-bis(2-aminopropyl)polypropylene oxide with molar weight of 400 $g{\cdot}mol^{-1}$ (PPO400, CAS no. 9046-10-0), 3-(isocyanatopropyl)triethoxysilane (IsoTrEOS, 95%, CAS no. 24801-88-5), hydrochloric acid (HCl, 37%, CAS no. 7647-01-0), sodium diclofenac (SDCF, CAS no. 15307-79-6), and potassium phosphate monobasic (KH_2PO_4, CAS no. 7778-77-0) were purchased from Sigma-Aldrich. The anhydrous solvents acetone (CAS no. 67-64-1), diethyl ether (CAS no. 60-29-7), and ethyl alcohol (CAS no. 64-17-5) were purchased from VWR and were used as received.

2.2 Synthesis of $CoFe_2O_4$ nanoparticles

The $CoFe_2O_4$ SPN was synthesized according to a method reported previously.[27] Briefly, an aqueous mixture of $Co(NO_3)_2$ and $FeCl_3$, in a 1:2 molar ratio, was prepared at a total concentration of 0.10 $mol{\cdot}L^{-1}$. An aqueous NaOH solution (10 $mol{\cdot}L^{-1}$) was then added, under vigorous stirring, to increase the pH to 13. The mixture was stirred for 1 h at 100 ºC before adding sufficient aqueous $Fe(NO_3)_3$ solution to give a Co^{2+}/Fe^{3+} molar ratio of 1:3. The precipitate obtained after the suspension temperature naturally reached 25 ºC was isolated, washed several times with acetone and diethyl ether, and finally dispersed in an aqueous solution of nitric acid (0.01 $mol{\cdot}L^{-1}$). The colloidal $CoFe_2O_4$ suspension used in this work was diluted to 1.45% (w/w) in nitric acid (0.01 $mol{\cdot}L^{-1}$).

2.3 Synthesis of ureasil-polyether-$CoFe_2O_4$ nanocomposites

In the first step of the synthesis, the covalently bonded OIH precursor ($(OEt)_3Si$-(polyether)-$Si(OEt)_3$) was prepared from the reaction between the amino-terminal groups of the PEO1900 or PPO400 macromers and the isocyanate groups of the IsoTrEOS crosslinker, at a molar ratio of 1:2 in ethyl alcohol, under reflux for 6 h at 78 ºC.[11,28] The hybrid precursor solutions were stored in closed flasks, at room temperature, in a dry environment. In the next step, SDCF (0.005 g) was solubilized in 0.5 mL of PEO1900 or PPO400 hybrid precursor solution under magnetic stirring, resulting in a 2.7 % (w/w) SDCF loading. Subsequently, 75 µL of aqueous HNO_3 solution (0.56 $mol \cdot L^{-1}$) was added to promote the sol-gel reaction of the $Si(OEt)_3$ groups present at both ends of the macromer chains, followed by the addition of 0.295 mL of a colloidal suspension of the $CoFe_2O_4$ SPN (1.45% w/w), resulting in a nanocomposite with 2.15% (w/w) of nanoparticles. The choice of $CoFe_2O_4$ concentration was made based on the temperature variation achieved by UPEO-based nanocomposites containing (0.5-5% w/w) $CoFe_2O_4$ SPN after application of an AMF for ~10 min (Figure S5, Supporting Information). The nanocomposite containing 2.15% (w/w) SPN reached the desirable temperature range (~42-46 ºC) for biomedical application.

In the case of the samples without $CoFe_2O_4$ (also denoted hybrids), 0.295 mL of aqueous HNO_3 solution (0.01 $mol \cdot L^{-1}$) was added (see Scheme 1). For the gelation step, the samples were maintained in a cylindrical mold for 48 h, at room temperature, resulting in monolithic xerogels (~ 0.5 mm thickness and weight of 0.2 g). The ureasil-polyether hybrids and the nanocomposites containing $CoFe_2O_4$ were denoted U-y and U-y-CoFe, respectively, where y represents the hybrid matrix (PEO or PPO).

Scheme 1. Schematic illustration of the synthesis of the ureasil-polyether hybrids and the nanocomposites containing $CoFe_2O_4$ SPN.

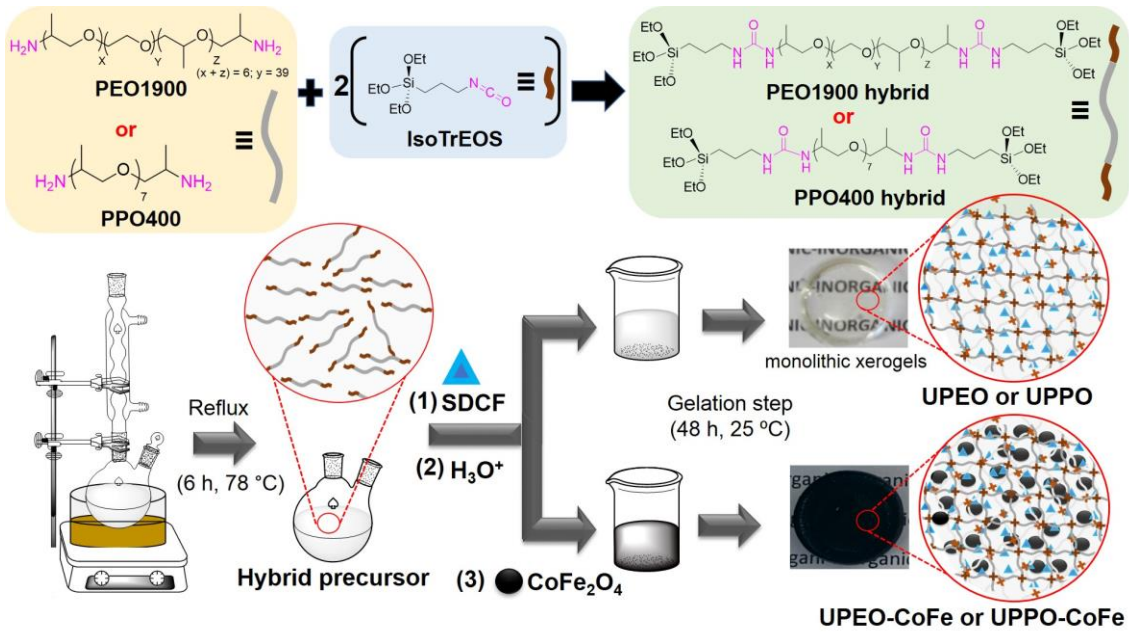

2.4 Characterization

Infrared spectra were recorded using a Fourier transform infrared (FTIR) spectrophotometer (Vertex 70, Bruker) equipped with a diamond crystal attenuated total reflectance (ATR) accessory and operated using 64 scans (4 cm^{-1} resolution) between 450 and 3000 cm^{-1}.

Transmission electron microscopy (TEM) images of the $CoFe_2O_4$ SPN and the nanocomposites were obtained using a JEOL JEM 100CX TEM instrument, while their high-resolution TEM (HRTEM) and selected area electron diffraction (SAED) images were obtained with a JEOL JEM 2011 TEM instrument. A diluted SPN suspension droplet was deposited onto a copper grid coated with carbon, and the excess was removed using filter paper. The nanocomposite samples were macerated, suspended in water, and deposited onto copper grids. The morphologies and size distributions of the $CoFe_2O_4$ particles/aggregates were analyzed using ImageJ software.[29] For SAED image, the diffraction rings were assigned to d_{hkl} spacings from the equation $d_{hkl} \cdot R_i = L \cdot \lambda$, where R_i is the radius of the ring, L is the camera length, and λ is the wavelength of the electron

beam. The camera constant ($L \cdot \lambda = 5.64 \times 10^{-8}$ cm^2) was determined using the SAED image of cubic-face-centered nanocrystalline gold as standard.

The crystalline features of the $CoFe_2O_4$ SPN, UPEO hybrid, and UPEO-CoFe nanocomposite were evaluated by X-ray diffraction (XRD), using a diffractometer (D5000, Siemens) operated with monochromatic Cu Kα radiation, with λ = 1.5418 Å selected by a curved graphite monochromator. The measurements were made in the 2θ range from 10° to 80°, with a step size of 0.02°/3 s^{-1}. The diffraction peaks were indexed using Crystallographica Search-Match software.[30]

The nanoscopic structures of the nanocomposites were evaluated by small-angle X-ray scattering (SAXS) measurements recorded at room temperature (25 ºC) at the SAXS beamline of the National Synchrotron Light Laboratory (LNLS, Campinas, Brazil). The beamline was equipped with a silicon-W/B4C toroidal multilayer mirror that focused the monochromatic X-ray beam (λ = 1.488 Å) onto the 2D photon-counting pixel detector (Pilatus 300k), located at 903.61 mm from the sample, resulting in a q-range spanning from 0.13 to 5.3 nm^{-1}.

Differential scanning calorimetry (DSC) measurements were carried out using a Q100 calorimeter (TA Instruments) operated at a heating rate of 10 ºC min^{-1}, under an atmosphere of N_2 at a flow rate of 50 mL·min^{-1}. The samples (~12 mg) were placed in a 40 µL hermetic aluminum pan and heated from -80 to 150 ºC. The DSC measurements were also used to determine the specific heat capacities (C_P) of the samples at 30 ºC, calculated using Equation 1:

$$C_p = \frac{K \cdot \Delta y_{(sample-BL)}}{dT/_{dt} \cdot m_{sample}} \quad (1)$$

where K is the calorimeter sensitivity, $\Delta y_{(sample-BL)}$ is the difference between the baseline and sample heat flow signals, dT/dt is the heating rate, and m_{sample} is the sample mass.[31]

Magnetization measurements of the $CoFe_2O_4$ colloidal suspension and nanocomposites were performed using a Quantum Design PPMS vibrating sample magnetometer (VSM) operating at 40 Hz.[32] The magnetization curves were obtained at 25 °C with a magnetic field (H) varying from -40 kOe to 40 kOe and normalized to 1.0 g of $CoFe_2O_4$ SPN. Magnetic hyperthermia (MH) measurements were performed using a DM100 instrument (nanoScale Biomagnetics) operated using an alternating magnetic field (AMF) with field amplitude (H) of 14.9 $kA \cdot m^{-1}$ and frequency (f) of 420 kHz. The MH curves were recorded at 25 ºC, and the temperature variations were monitored with a fluoro-optic fiber thermometer.

The contact angle measurements of the samples were performed in an OCA15 instrument (Dataphysics) in sessile drop mode at 20 °C. A drop of deionized water (7.0 μL) was dispensed (rate = 1.32 $\mu L\ s^{-1}$) on the surface of the monoliths, and the values of the air-water-solid contact angles were monitored for 10 min from images obtained. The contact angle values were obtained using proprietary software (Dataphysics), where the shape of the drop is described by the Young-Dupré equation, assuming a smooth and homogeneous surface.[33]

2.5 Drug release assays

The *in vitro* drug release assays were performed with SDCF-loaded materials immersed in 50 mL of phosphate buffer solution (pH 7.2) at 37 ºC. The temporal evolution of SDCF release was monitored by absorbance measurements recorded in the wavelength range 200-400 nm, using a UV-Vis spectrometer (Cary 60, Agilent Technologies) fitted with a quartz cuvette (1.0 cm optical path length). Quantitative determination of the cumulative SDCF release was performed using a

calibration curve constructed using the maximum absorbance values at 276 nm of SDCF standard solutions at different concentrations (Figures S1a-b, Supporting Information).

The amounts of leached $CoFe_2O_4$ SPN from nanocomposites during the drug release assays were measured with an atomic absorption spectrometer (PinAAcle 500, Perkin Elmer) after ~16h of immersion of the monoliths in 100 mL of phosphate buffer solution (pH 7.2) at 37°C. For the analysis, 5 mL of the buffer solution containing the leached $CoFe_2O_4$ SPN was pretreated with small volumes of concentrated HNO_3 (0.1 mL) and HCl (0.05 mL) aqueous solutions until total dissolution of the SPN into iron (III) and cobalt (II). Metal ion concentrations were determined by measuring the absorbance of the atomized solutions in flame at λ =248.3 nm (Fe) and 240.7 nm (Co).[34] These measurements were performed in quadruplicate.

3. RESULTS AND DISCUSSION

3.1 Structural characteristics

The FTIR spectrum of the $CoFe_2O_4$ SPN (Figure S2, Supporting Information) presented bands at around 594 and 414 cm^{-1}, assigned to stretching vibration of Fe^{3+}-O^{2-} at tetrahedral and octahedral sites, respectively, in the spinel structure of the $CoFe_2O_4$.[35] The cubic spinel structure (JCPDS card #22-1086) of the nanoparticles was confirmed from SAED pattern of TEM-HRTEM images of the $CoFe_2O_4$ powder (Figures S3a-d and Table S1, Supporting Information). The morphology of the $CoFe_2O_4$ nanoparticles, revealed from the TEM (Figure S4a, Supporting Information), showed the presence of nearly isometric particles with well-defined faceted shapes. The size histograms obtained from the TEM image (Figure S4b, Supporting Information) were fitted using a log-normal distribution function and showed a monomodal distribution with an average size of 8.9 ± 0.5 nm.

The incorporation of $CoFe_2O_4$ SPN in the hybrid matrices to obtain UPEO-CoFe and UPPO-CoFe nanocomposites did not change the morphology and size of the nanoparticles (Figures 1a and 1b, respectively). The $CoFe_2O_4$ particles showed uniform size distributions with average nanoparticle sizes of 8.1 ± 0.2 and 8.9 ± 0.2 nm for UPEO-CoFe (Figure 1c) and UPPO-CoFe (Figure 1d), respectively. The characteristic peaks of $CoFe_2O_4$ in the XRD pattern of nanocomposites (Figure S6, Supporting Information) evidenced the conservation of the crystalline phase of the SPN in both hybrid matrices.

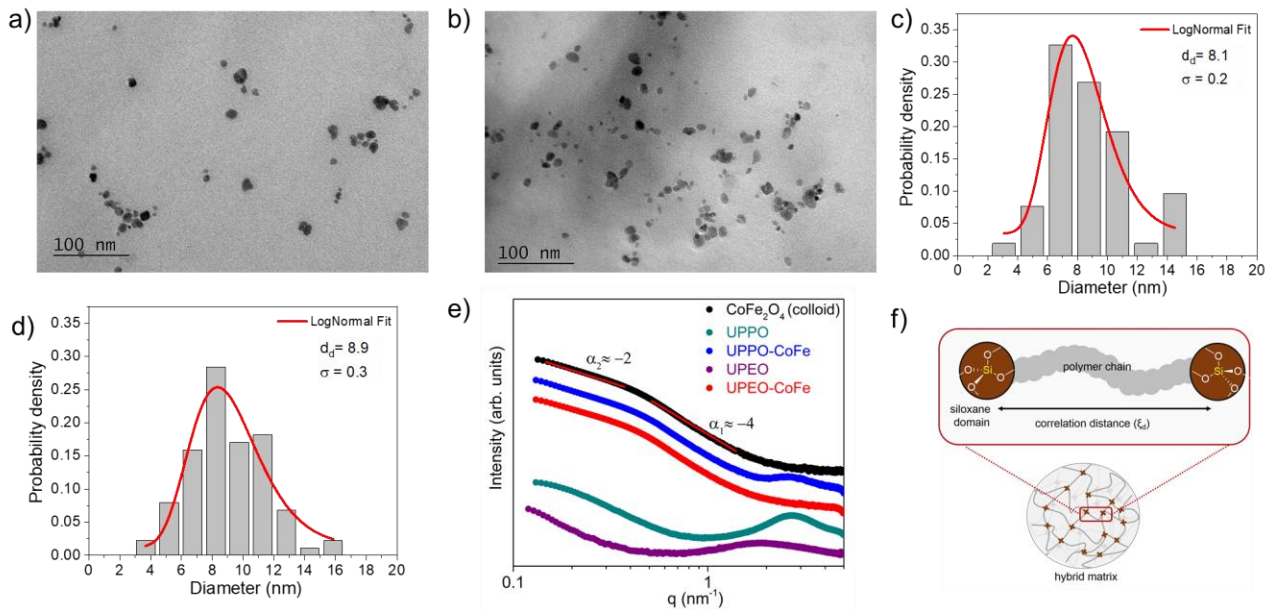

Figure 1. TEM images of (a) ureasil-poly(ethylene oxide) and (b) ureasil-poly(propylene oxide) nanocomposites containing 2.15% (w/w) $CoFe_2O_4$ SPN, and the corresponding particle size distribution histograms fitted with log-normal functions (red lines) shown in (c) and (d), respectively. (e) SAXS curves for the $CoFe_2O_4$ colloidal suspension, the SDCF-loaded ureasil-polyether hybrids, and the nanocomposites containing 2.15% (w/w) $CoFe_2O_4$ SPN. (f) Schematic representation of the correlation distance between the siloxane crosslinking nodes in the ureasil-polyether hybrids.

Information concerning the nanoscopic structures of the $CoFe_2O_4$ SPN, the hybrids, and the composites was obtained from SAXS measurements (Figure 1e). The SAXS curve for the $CoFe_2O_4$ colloidal suspension (black line) presented a Gaussian decay in the middle q region, with an asymptotic linear trend having a slope (α_1) of -4. This behavior was in agreement with the classical Porod law ($I(q) \propto q^{-4}$), indicating that the two-electron density model was satisfied and that the interface between the round primary nanoparticles and the dispersion medium was well-defined and without heterogeneities.[36] The SAXS curves for a diluted set of non-interacting particles usually present a Gaussian decay in the middle q region, with a plateau in the low q region, also known as the Guinier region.[36] Here, the presence of a linear dependent region (α_2 of -2), instead of a plateau at low q, indicated the formation of small aggregates.[37]

The SAXS curves for the UPEO and UPPO hybrids exhibited a single broad peak with maxima centered at 1.83 and 2.70 nm^{-1}, respectively. This correlation peak evidenced a strong spatial correlation between the siloxane crosslinking nodes in the hybrid matrix (represented in Figure 1b). The average correlation distances (ξ_d) between two adjacent nodes, given by $\xi_d = 2\pi/q_{max}$ (where q_{max} is the modulus of the scattering vector at the peak maximum),[11] were 3.4 and 2.3 nm for the UPEO and UPPO hybrids, respectively. The greater value of ξ_d for the UPEO hybrid could be explained by the larger chains of the high molecular weight PEO (1900 $g \cdot mol^{-1}$) compared to the chains of the low molecular weight PPO (400 $g \cdot mol^{-1}$). However, there was a decrease in the intensity of the correlation peak for the UPPO-CoFe nanocomposite and complete disappearance of this peak for UPEO-CoFe, which could be explained by the greater electronic contrast due to the $CoFe_2O_4$ SPN, as compared to the siloxane crosslinking nodes of the hybrid matrices.[23] This implied that the correlation peak resulting from the siloxane nodes was obscured by the high scattering power of the $CoFe_2O_4$ SPN.

The shapes of the SAXS curves for the ureasil-polyether nanocomposites containing $CoFe_2O_4$ SPN were similar to that for the colloidal suspension, with I (q) ∝ q^{-4} in the middle q region and a linear dependent region (slope of ~ -2) in the low q region. These indicated no substantial alteration of the initial state of aggregation of the nanoparticles when they were inserted in the hybrid matrices, which agreed with the TEM images. This was an important finding because the state of aggregation can influence the heating capacity of SPN, in some instances resulting in a decrease in hyperthermia efficiency.[38]

FTIR spectroscopy was also used to assess the interaction of the $CoFe_2O_4$ SPN with the hybrid matrices by analyzing the characteristic bands of the ureasil-polyether material (Figure 2), which appear in two main spectral ranges.[39–41] Between 1800 and 1500 cm^{-1}, the amide I (at around 1647 cm-1) and amide II (at 1554 cm-1) bands of the urea linkage are assigned to υ C=O stretching vibration in different environments and to δ NH in-plane bending vibrations, respectively. In the region from around 1500 to 900 cm^{-1}, bands correspond to the macromer backbone at around 1452, 1092, and 1037 cm^{-1}, assigned to δ CH_3 bending, υ C-OC stretching, and ρ CH_2 rocking modes, respectively. The first region can provide information regarding intermolecular hydrogen bonding involving the urea linkage, while the second region is more sensitive to conformational changes that occur in the polymer chain.[40] Siloxane group vibration modes (ν Si-O-Si and ν C-Si-O) usually appear in the range 1000-1150 cm^{-1} but are enveloped by the strong band of the ether group (C-O-C).[40] The characteristic bands of SDCF (Figures S7a and S7b, Supporting Information) were obscured by the PEO and PPO bands due to a low percentage of SDCF loading. However, in the case of higher SDCF loaded hybrids the interaction of SDCF with the ureasil-polyether matrix mainly involves the amine and carbonyl groups of the SDCF molecule with the urea groups present at the end of the polymeric chains.[42]

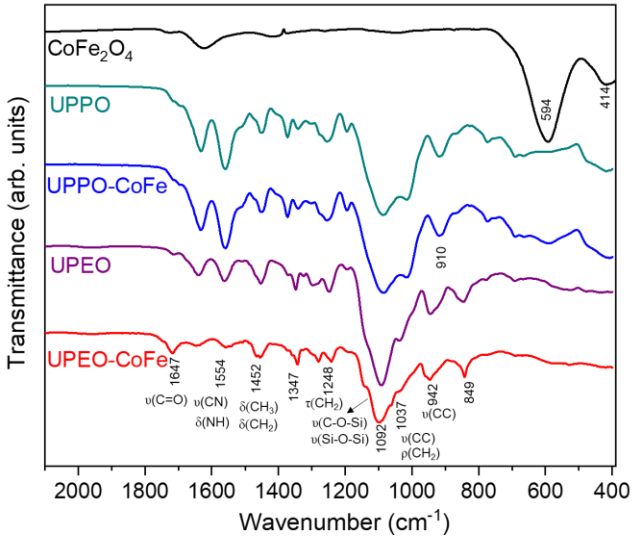

Figure 2. FTIR spectra in the range from 2100 to 800 cm^{-1} for the ureasil-polyether hybrids and the nanocomposites containing 2.15% (w/w) $CoFe_2O_4$ SPN.

No appreciable changes were observed for the characteristic vibration modes in the FTIR spectra of the ferrite nanocomposites (UPEO-CoFe and UPPO-CoFe) compared to the UPEO and UPPO hybrids. This suggested that the $CoFe_2O_4$ SPN were incorporated into the hybrid matrices without specific interaction with the functional groups of the PPO400 or PEO1900 macromer and without promoting appreciable changes in the conformation of the organic chains. It was also not possible to find evidence of interaction between the SPN and the hybrid matrix from HRTEM images of the nanocomposites (Figures S8a and S8b, Supporting Information).

3.2 Thermal characteristics

The DSC curves (Figure 3) for the PEO based samples (UPEO and UPEO-CoFe) showed an endothermic event at 15-40 ºC, corresponding to the first-order reversible thermal transformation (crystallization ↔ melting) of PEO1900. PEO with a molecular weight greater than 1000 $g{\cdot}mol^{-1}$ is semicrystalline, with a mesoscopic scale structure consisting of amorphous and lamellar

crystalline regions that melt above the melting temperature (T_m). This endothermic peak was not present in the DSC curves for the PPO based samples since PPO400 is amorphous. For PEO based samples (at -60 to -30 ºC) and PPO based samples (at 15 to 35 ºC), it was observed the reversible a change in heat capacity (ΔC_p) characteristics of the second-order transition (glass ↔ rubber) of the amorphous region of the polymer, which occurs around a glass transition temperature (T_g). [43]

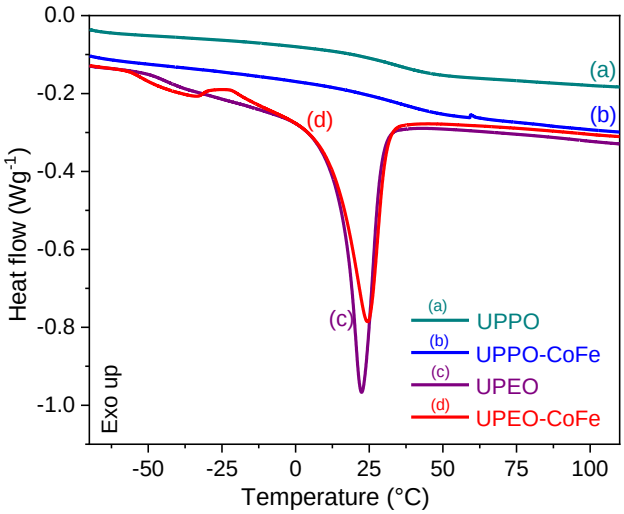

Figure 3. DSC curves for the SDCF-loaded ureasil-polyether hybrids and the nanocomposites containing 2.15% (w/w) $CoFe_2O_4$ SPN.

The endothermic peaks in the DSC curves were used to determine T_m and the degree of crystallinity (D_c) of the PEO based samples, using the following equation:

$$D_c = \frac{\Delta H_f}{\Delta H_p} \cdot 100 \qquad (2)$$

where, ΔH_f is the melting enthalpy of the semicrystalline PEO in the hybrid, obtained by integrating the endothermic peak, and ΔH_p is the melting enthalpy of a 100% crystalline PEO (ΔH_p

= 188.9 J·g^{-1}).[44] Table 1 shows the values of T_g, T_m, and D_C obtained from the analysis of the DSC curves.

Table 1. Thermal properties determined by DSC measurements.

Samples	**T_m (ºC)**	**D_c (%)**	**T_g (ºC)**	**C_p (J·g^{-1}·ºC^{-1})**
UPEO	22	23	-49	2.61 ± 0.28
UPEO-CoFe	24	21	-55	2.88 ± 0.47
UPPO	-	-	22	1.53 ± 0.02
UPPO-CoFe	-	-	18	2.09 ± 0.02

The small difference in T_m and D_c parameters resulting from the presence of the $CoFe_2O_4$ SPN in the UPEO-CoFe nanocomposite (24 ºC and 21%), compared to the UPEO hybrid (22 ºC and 23%), indicated that the nanoparticles did not interact strongly with the ether-type oxygen atoms of the polyether chains, in agreement with the FTIR results. It is well known that the most significant changes observed in PEO crystallization occur due to the dissolution of small metallic cations.[45,46] The solvation of these cations by the ether-type oxygen atoms is sufficiently strong to induce an "ether crown" conformation, which hinders or prevents the PEO chains from adopting the helical conformation typically found in the crystalline domains of PEO.[45,46] According to the experimental results, this was not effective in the case of the interactions of the PEO chains with the surfaces of the $CoFe_2O_4$ nanoparticles. Similar behavior was observed elsewhere for the conjugation of 3 nm cerium nanoparticles with the ureasil-poly(ethylene oxide) matrix.[16]

T_g values showed a significant decrease, from −49 °C (UPEO) to −55 °C (UPEO-CoFe), and from 22 °C (UPPO) to 18 °C (UPPO-CoFe) with the incorporation of $CoFe_2O_4$ SPN in the PEO matrix, evidencing the reduction of rigidity of polymer chains. This feature indicates the absence of cohesive interaction between the SPN and the polymeric amorphous phase of the hybrid matrix.

The formation of strong chemical interactions between nanofillers and polymeric/hybrid matrices is usually accompanied by an increase in T_g due to the increased rigidity of the polymeric phase.[47–49] Moreover, it is known that the addition of spherical nanofillers (<10% w/w) to a low interacting polymeric matrix can cause an increase of the free volume, which increases the mobility of the chains, consequently assisting the thermal transition.[50,51] In the case of matrices composed of long polymer chains, the presence of nanoparticles can also have a disentangling effect, leading to faster segmental dynamics.[50,51] However, such entanglements are not expected for PEO based samples prepared with PEO chains of low molecular weight (MW = 1900 $g \cdot mol^{-1}$).[52]

The DSC measurements were also used to determine the specific heat capacity (C_P) of the samples at 30 ºC (shown in Table 1), using Equation 1. For the UPPO-CoFe nanocomposite (C_p = 2.09 ± 0.02 $J \cdot g^{-1} \cdot ºC^{-1}$) and UPEO-CoFe nanocomposite (C_p = 2.88 ± 0.47 $J \cdot g^{-1} \cdot ºC^{-1}$), the C_p values were slightly higher compared to hybrids. The calorific capacities of nanocomposites did not follow a rule of mixtures ($C = C_m.\varphi_m + C_{co}.\varphi_{co}$), where C_m and φ_m represent the specific heat and mass fraction for the hybrid matrix, and C_{co} and φ_{co} represent these parameters for $CoFe_2O_4$. The C_P values would be lower for both nanocomposites considering that the calorific capacity of $CoFe_2O_4$ (0.65 $J \cdot g^{-1} \cdot ºC^{-1}$) [53] is lower than that of the hybrid matrix.

The specific heat of a polymeric material is related to the storage of kinetic energy involving the polymer chains' vibrational modes and rotational movements, which are individually considered degrees of freedom.[43] Therefore, the greater the number of degrees of freedom of the polymer chains, the greater the specific heat of the material.[43] In this way, the increased specific heats of the nanocomposites after the addition of $CoFe_2O_4$ SPN supported the hypothesis that the dispersion of the nanofillers in the non-crystalline regions of the PEO and PPO matrices increased the free volume in the nanocomposites. It could be inferred that this increase in free volume favored the

rotational movements of the PEO and PPO chains, consequently increasing the degrees of freedom of these chains. As discussed in the next section, the differences in the C_p values and thermal behaviors of the UPEO-CoFe and UPPO-CoFe nanocomposites had a clear influence on the temperature variation achieved in magnetic hyperthermia.

3.3 Magnetic behavior

The magnetization curves M(H) for the colloidal suspension of $CoFe_2O_4$ SPN and nanocomposites (Figure 4a) were typical of superparamagnetic or ferrimagnetic samples, with high magnetic susceptibility, and a strong saturation magnetization (M_s) reached at low field. Sigmoid-shaped magnetization curves without hysteresis usually evidence the superparamagnetic behavior of magnetic materials. [54] Particles smaller than a specific critical size have magnetic monodomains whose moments align in the direction of the applied field. When the field is removed (H = 0), the magnetization becomes null, leading to a coercive field (H_c) and the remaining magnetization (M_R) also null.[54] The critical size for superparamagnetism to occur depends on the material, and for $CoFe_2O_4$ this size is in the range of 5 to 9 nm.[54,55] The M(H) curves were superimposed after their normalization based on the experimental values of M_S and using a value [27] of m_s for the pure $CoFe_2O_4$ SPN of 62 emu g^{-1} considering the weight percent of the SPN ($w_{CoFe2O4} = M_S/m_s \times 100$).

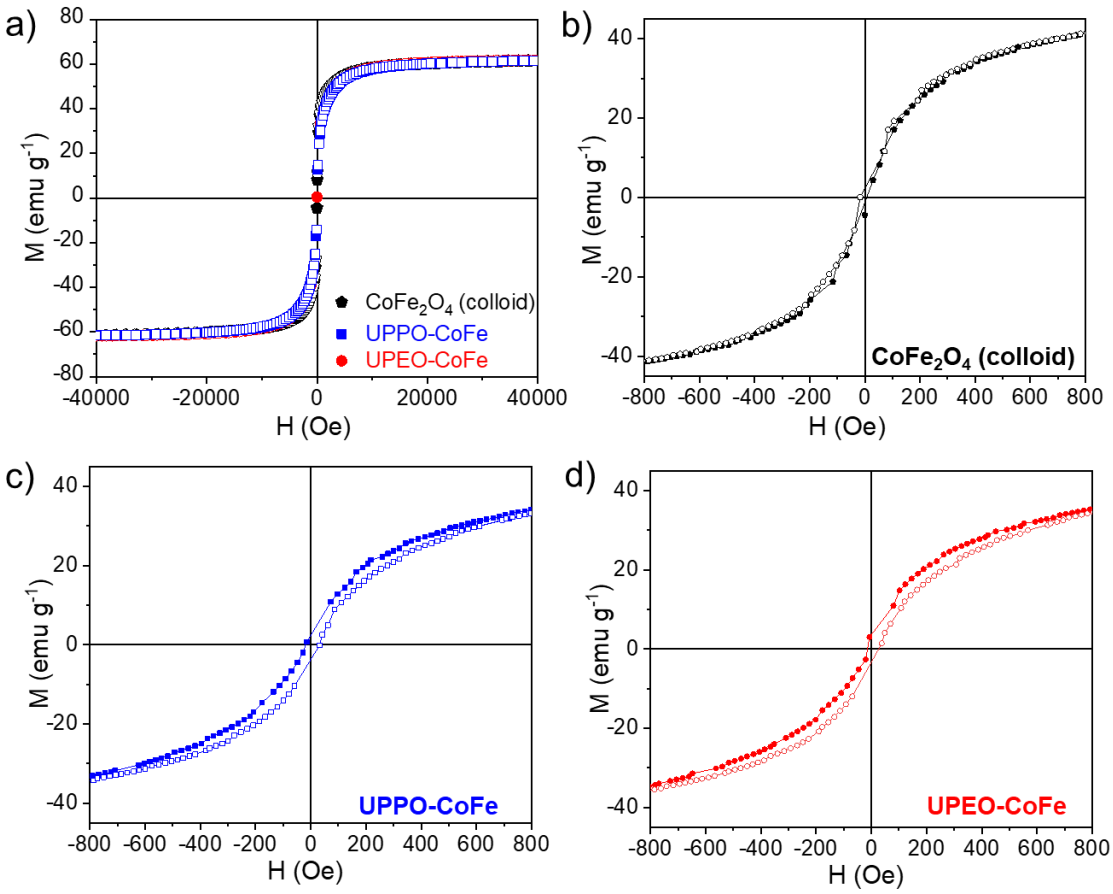

Figure 4. (a) Magnetization curves at 25 ºC for the $CoFe_2O_4$ colloidal suspension and SDCF-loaded ureasil-polyether nanocomposites containing 2.15% (w/w) $CoFe_2O_4$ SPN in the field range -4000 to 4000 Oe. Enlargements at low field (-800 to 800 Oe) of the magnetization curves for (b) $CoFe_2O_4$ colloidal, (c) ureasil-poly(propylene oxide) and (d) ureasil-poly(ethylene oxide) nanocomposites.

The three normalized curves are globally identical. However, a thorough examination of the curves at low field highlights some differences (Figures 4b-d). Indeed, the magnetization curve for the colloidal suspension did not present hysteresis, to the contrary of nanocomposite samples where a minimal hysteresis is evidenced by coercive field (Hc ≈ 40 Oe) and $M_R/M_s \approx 0.04$ (where M_R is remanent magnetization). The apparent and perfect superparamagnetic behavior of the

colloidal suspension is due to the Brownian motion of the SNP in water. For the nanocomposites, the Brownian motion was blocked by the rigidity of the PEO and PPO matrix. Then, the motion of the magnetic moment is only due to the Neel relaxation. [56,57] Nevertheless, this second motion can be slightly blocked for the larger SPN (representing a small SPN percentage). This is explained by their high anisotropy energy (E_a) resulting from their high volume conjugated to the strong magnetocrystalline anisotropy of $CoFe_2O_4$ SPN ($E_a = K \times V$, where K is the magnetic anisotropy constant, and V is the volume of the nanoparticle).[58] This induces a slight ferrimagnetic behavior for the nanocomposites.

Figure 5 presents the temperature profiles of the samples under the application of an AMF. The UPEO and UPPO hybrids did not show heating under AMF due to the absence of $CoFe_2O_4$ SPN in the hybrid matrix. The curves of $CoFe_2O_4$ colloidal suspension and the UPEO-CoFe and UPPO-CoFe nanocomposites had a similar shape, with a strong temperature enhancement at the beginning of the process, which tended asymptotically to a constant value after a long time, due to decrease of the heating rate caused by the competition between the cooling effect of the external bath and the heating effect of the AMF.[57]

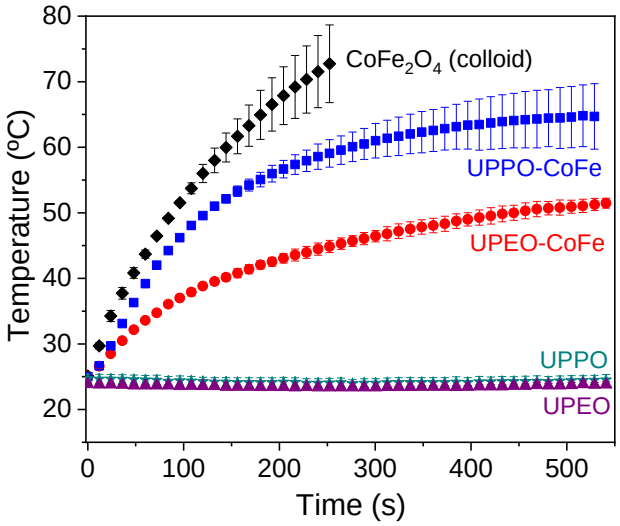

Figure 5. Temperature increases due to magnetic hyperthermia (H = 14.9 kA·m^{-1}; f = 420 kHz) for the colloidal suspension of $CoFe_2O_4$ SPN (1.5% w/w in aqueous solution at pH 2.0) and the SDCF-loaded ureasil-polyether hybrids and the nanocomposites containing 2.15% (w/w) $CoFe_2O_4$ SPN.

Differences in the asymptotic temperature were observed among the three samples, with the greatest temperature enhancement recorded for the colloidal suspension, followed by the UPPO-CoFe and UPEO-CoFe nanocomposites. The temperature increases (ΔT) achieved during the initial 240 s of application of the AMF were 47, 34, and 20 ºC for the $CoFe_2O_4$ suspension, UPPO-CoFe, and UPEO-CoFe, respectively (Table 2). The influence of the hybrid matrix on the heating effect of the SPN under AMF was evaluated using the specific loss power (SLP) (Table 2), defined as the energy dissipation efficiency of superparamagnetic nanoparticles per mass of magnetic material. The SLP values were calculated as follows:

$$SLP = C_p \cdot \frac{m_{sample}}{m_{SPN}} \cdot \left(\frac{dT}{dt}\right)_{max} \quad (3)$$

where, C_p is the sample heat capacity, m_{sample}/m_{SPN} is the ratio between the sample mass and the magnetic $CoFe_2O_4$ SPN mass, and $(dT/dt)_{max}$ is the maximum heating rate (Table 2) obtained by applying a Box-Lucas fit to the magnetic hyperthermia curves (as shown in Figure S9, Supporting Information).[59] SLP calculations using the Box-Lucas method are more accurate compared to other methods.[60] For the colloidal suspension of the $CoFe_2O_4$ SPN, the water heat capacity (C_p = 4.18 J·g^{-1}·ºC^{-1}) was assumed, while C_p for the nanocomposites was obtained from the DSC results (Table 1).

Table 2. Experimental data obtained from the hyperthermia measurements.

Samples	ΔT in 240 s (ºC)	$(dT/dt)_{max}$ (ºC s^{-1})	SLP (W g^{-1})
$CoFe_2O_4$ (colloidal)	47 ± 6	0.344 ± 0.012	99 ± 9
UPPO-CoFe	34 ± 5	0.302 ± 0.022	29 ±5
UPEO-CoFe	20 ± 2	0.151 ± 0.008	20 ± 3

The SLP values for UPEO-CoFe and UPPO-CoFe were about five-fold and three-fold lower, respectively, compared to the SLP value for colloidal $CoFe_2O_4$. The decrease of SLP has previously been attributed to the formation of aggregates, resulting in strong interactions among the nanoparticles.[38] In the present case, the SAXS results confirmed that the aggregation state of the SPN in aqueous suspension was not affected by their conjugation to the hybrid matrices. Therefore, the overall decrease of SLP observed for both nanocomposites compared to the colloidal $CoFe_2O_4$ could be explained by the inhibition of Brownian relaxation (immobilization effect), leading to decreased energy dissipating the power of the $CoFe_2O_4$ SPN when immobilized in polymer nanocomposites.[56,57] This hypothesis was supported by Engelmann et al., who observed that the heating capacity of magnetic nanoparticles immobilized in acrylamide hydrogels depended on the crosslinking node distances (mesh size). Since the lowest SLP value was measured for the sample with the smallest mesh size, it was concluded that decrease of the mesh size caused a strong inhibition of Brownian relaxation, consequently affecting the heat capacity of the SPN.[61]

The difference between the two nanocomposites in terms of ΔT reached after 240 s of AMF indicated that the UPPO-CoFe provided better performance for MH. This could be explained by the lower heat capacity at 30 ºC and consequently the higher SLP of the SPN in the UPPO-CoFe, compared to the UPEO-CoFe. The difference in the calorific capacity of the nanocomposites was

due to the difference in the thermal behavior of the PEO1900 (semicrystalline) and PPO400 (amorphous) matrices at room temperature. However, it should be noted that the two nanocomposites achieved significant ΔT during the application of AMF and that both are potential candidates as bifunctional systems for drug delivery and MH.

3.4 Wettability, drug release, and leaching

The effect of the hydrogel of PEO based samples on the temporal evolution of the surface wettability was evaluated by measuring the contact angle at different times (θ_{tmin}) (Figure 6a and 6b). The θ values for UPPO (θ_{0min} = 78.3 ± 6.4°) and UPPO-CoFe (θ_{0min} = 73.6 ± 6.1°) referring to the initial time of the assay remained unchanged after 10 min, while for UPEO (θ_{0min} = 61.0 ± 5.4° to θ_{10min} = 44.2 ± 5.0°) and UPEO-CoFe (θ_{0min} = 67.6 ± 1.4° to θ_{10min} = 41.8 ± 1.9°) there was a decrease in θ values with time. This difference in wettability arose due to the known hydrophilic behavior of the PEO and hydrophobic nature of the PPO.[12,20] The decrease in the θ values for the PEO based samples is related to easily water spreading on the surface induced by the water uptake into the UPEO three-dimensional networks based on hydrophilic PEO chains. [14 18] The time evolution of θ can be considered an indirect measure of the water uptake profile for the PEO based samples, since swelling played an essential role in the release process of the drug incorporated into the hybrid matrix.

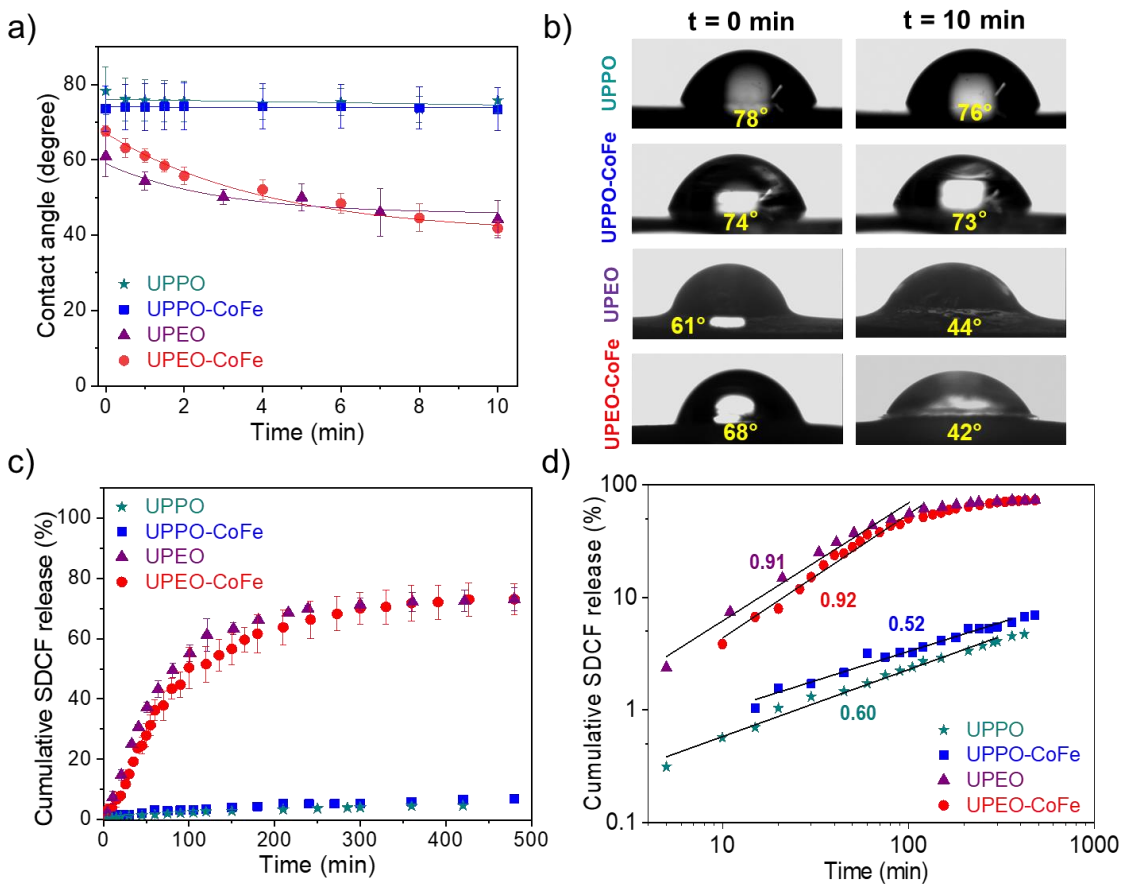

Figure 6. (a) Temporal evolution of contact angle and (b) Images of the air-water-solid interface at 0 min and 10 min after water drop dispersion for ureasil-polyether hybrids and the nanocomposites containing 2.15% (w/w) $CoFe_2O_4$ SPN. (c) Temporal evolution and (d) Log-log plots of cumulative SDCF release in phosphate buffer (pH 7.2), at 37 ºC from the ureasil-polyether hybrids and the nanocomposites containing 2.15% (w/w) $CoFe_2O_4$ SPN.

Figure 6c shows the temporal evolution of cumulative SDCF release from the ureasil-polyether hybrids and nanocomposites in phosphate buffer (pH 7.2) at 37 ºC. The curves demonstrated that the SDCF release profile was dependent on the hydrophilicity of the hybrid matrix. The PEO samples (hydrophilic hybrid matrix) showed a rapid release profile during the first two hours of monitoring, followed by a plateau, while the PPO samples (hydrophobic hybrid matrix) showed

moderate and sustained release. After 8 h, the amounts of SDCF released from the UPEO and UPPO hybrids were 73 and 5%, respectively.

The release of different drugs incorporated in ureasil-polyether hybrids is strongly dependent on the hydrophilicity and swelling capacity of the material.[12,42] The hydrophilic nature of the PEO polymer chains allows rapid water uptake by the hybrid matrix, leading to a swelling degree of 300% in approximately 1 h of immersion in an aqueous medium. [12,62] The uptake of water into the hybrid matrix from the surrounding environment promotes the dissolution of the incorporated drug, with the release being governed by a diffusion process.[42] In contrast, for UPPO hybrids, the uptake of water into the matrix is a prolonged process due to the hydrophobic nature of the PPO polymer.[12,22] It is important to note that both nanocomposites showed release profiles compatible with their hybrid matrices, indicating that the conjugation of the $CoFe_2O_4$ SPN (2.15% w/w) did not create a physical barrier or an alternative path for the release of the SDCF.

The kinetic mechanism for release of the SDCF from the nanocomposites was investigated by applying the semi-empirical power-law model proposed by Korsmeyer *et al*.[63] (Equation 4) to the experimental data:

$$\frac{M_t}{M_\infty} = kt^n \tag{4}$$

where, M_t/M_∞ is the cumulative fraction of the drug released at time t, k is a release constant that considers structural and geometric characteristics of the matrix, and the exponent n describes the release mechanism. The power-law dependency predicted by Equation 4 can be confirmed by the existence of a linear trend in a log-log plot (Figure 6d). The slope extracted from this linear trend provides the value of n, which here indicated that the mechanism of release from UPEO and

UPEO-CoFe was anomalous transport (n = 0.9), while the release from UPPO and UPPO-CoFe was by classical Fickian diffusion (n = 0.5). The similar values of n for the nanocomposites and hybrids confirmed that the $CoFe_2O_4$ SPN in both PEO and PPO matrices did not affect the SDCF release mechanisms.

The influence of higher concentrations of $CoFe_2O_4$ SPN on the release of SDCF was evaluated by preparing UPEO-CoFe and UPPO-CoFe nanocomposites containing 5% (w/w) $CoFe_2O_4$. The amounts of SDCF released from these samples (Figure S10a, Supporting Information) were very similar to the quantities released from the nanocomposites containing 2.15% (w/w) $CoFe_2O_4$, showing that the incorporation of up to 5% (w/w) $CoFe_2O_4$ did not affect the SDCF release profile. In addition, the influence of AMF on the SDCF release profile was also assessed (Figure S10b, Supporting Information). In these assays, the application of AMF (H = 14.9 $kA \cdot m^{-1}$; f = 420 kHz) was carried out on eight occasions (equally spaced), each lasting 20 min. This AMF application regime did not influence the amount of SDCF released from the nanocomposites containing 2.15% (w/w) $CoFe_2O_4$ SPN. These experimental results demonstrated the emerging potential of these hybrid nanocomposites in the design of new bifunctional devices able to couple chemotherapy and magnetic hyperthermia without mutual interferences.

It is important to highlight that the monolithic nanocomposites remained intact during the SDCF release assays even after ~16 h immersed in an aqueous medium (Figures S11a and S11b, Supporting Information) and without macroscopic evidence of $CoFe_2O_4$ SPN leaching in aqueous medium. Nevertheless, we evaluated the $CoFe_2O_4$ SPN leaching by the atomic absorption of Fe and Co in phosphate buffer solution (pH 7.2) after ~16 h of the SDCF release assays. The percentage of SPN leached from UPEO-CoFe (3.4 ± 0.1 %) was ~17 times higher compared to UPPO-CoFe (0.20 ± 0.01 %). The rapid uptake of water by the hydrophilic PEO matrix of the

UPEO-CoFe nanocomposite can lead to the formation of microchannel cracks near to the surface of the monolithic body inducing the release of $CoFe_2O_4$ SPN. The low $CoFe_2O_4$ leaching indicate that the SPN remains satisfactorily trapped inside the bulk of both nanocomposites, even after immersion in aqueous media.

4. CONCLUSIONS

The incorporation of $CoFe_2O_4$ SPN (average size ~9 nm) in the organic-inorganic hybrid matrix (UPEO and UPPO) led to higher specific heat capacity. This effect was more pronounced for UPEO-CoFe ($C_p = 2.88 \pm 0.47$ $J \cdot g^{-1} \cdot °C^{-1}$), compared to UPPO-CoFe ($C_p = 2.09 \pm 0.02$ $J \cdot g^{-1} \cdot °C^{-1}$). Hence, the later was more effective for MH, since the temperature variation achieved with the application of AMF was 1.8 times higher than for the UPEO-CoFe nanocomposite.

The hydrophilic polymeric chains of UPEO network promoted much greater and faster drug delivery as compared to hydrophobic UPPO hybrid. The similar amounts of SDCF released from the hybrids and nanocomposites evidenced that the conjugation of $CoFe_2O_4$ SPN did not cause the creation of neither barrier nor alternative path for the release of SDCF. The results highlighted the importance of selecting the most appropriate hybrid matrix for MH using SPN/OIH nanocomposites, in addition to the effect of the SPN, which has been the focus of most studies involving these nanocomposites. The ureasil-polyether-$CoFe_2O_4$ nanocomposites can be designed as delivery systems coupled with magnetic hyperthermia. This bifunctionality has attracted attention to SPN/polymer nanocomposites, making them good candidates in several biomedical applications, such as scaffolds for tissue engineering or injectable magnetogels for cancer treatments.

ASSOCIATED CONTENT

The following files are available free of charge (PDF): (i) Sodium diclofenac analytical curve: Figure S1, absorbance spectra in the visible region for SDCF at different concentrations, and analytical curve; (ii) Characteristics of the $CoFe_2O_4$ nanoparticles and nanocomposites: Figure S2, FTIR spectrum of the $CoFe_2O_4$ nanoparticles; Figure S3, TEM image and SAED pattern of the $CoFe_2O_4$ nanoparticles; Figure S4, TEM images of $CoFe_2O_4$ nanoparticles and particle size distribution histograms; Figure S5, magnetic hyperthermia effects for ureasil-poly(ethylene oxide) nanocomposites containing (0.5-5% w/w) $CoFe_2O_4$; Figure S6, X-ray diffractograms of the $CoFe_2O_4$ nanoparticles, hybrids, and nanocomposites; Table S1, attribution of the main (hkl) reflections in SAED pattern; Figure S7, FTIR spectra for SDCF, SDCF-loaded and unloaded ureasil-polyether hybrids; Figure S8, HRTEM images of the nanocomposites; (iii) Determination of the maximum heating rates from the magnetic hyperthermia curves: Figure S9, representation of the initial slope of the magnetic hyperthermia curve and parameters obtained with the Box-Lucas model; (iv) Drug release from ureasil-polyether nanocomposites: Figure S10, temporal evolution of cumulative SDCF release from the ureasil-polyether nanocomposites under and without an external AMF; Figure S11, photograph of the nanocomposites.

AUTHORS INFORMATION

Corresponding Author

*Celso V. Santilli

E-mail: cv.santilli@unesp.br

Author Contributions

The manuscript was written with contributions from all the authors. All the authors have approved the final version of the manuscript.

Funding Sources

Fundação de Amparo à Pesquisa do Estado de São Paulo (FAPESP) and Conselho Nacional de Desenvolvimento Científico e Tecnológico (CNPq).

ACKNOWLEDGMENTS

This work received financial support from the following Brazilian agencies that promote scientific research: Fundação de Amparo à Pesquisa do Estado de São Paulo (FAPESP, grant #2017/07822-7) and Conselho Nacional de Desenvolvimento Científico e Tecnológico (CNPq, grants #482176/2013-0, #163588/2015-5, and #147402/2019-0). The authors are very grateful to Sandra Casale, David Hrabovsky and Delphine Talbot for their technical support.

ABBREVIATIONS

AMF, alternating magnetic field; ATR, attenuated total reflectance; DSC, differential scanning calorimetry; FTIR, Fourier transform infrared spectroscopy; MH, magnetic hyperthermia; OIH, organic-inorganic hybrid; SAXS, small-angle X-ray scattering; SDCF, sodium diclofenac; SLP, specific loss power; SPN, superparamagnetic nanoparticles; TEM, transmission electron microscopy; UPEO, ureasil-poly(ethylene oxide); UPPO, ureasil-poly(propylene oxide); XRD, X-ray diffraction.

REFERENCES

(1) Das, P.; Colombo, M.; Prosperi, D. Recent Advances in Magnetic Fluid Hyperthermia for Cancer Therapy. *Colloids Surfaces B Biointerfaces* **2019**, *174*, 42–55. https://doi.org/10.1016/j.colsurfb.2018.10.051.

(2) Périgo, E. A.; Hemery, G.; Sandre, O.; Ortega, D.; Garaio, E.; Plazaola, F.; Teran, F. J.

Fundamentals and Advances in Magnetic Hyperthermia. *Appl. Phys. Rev.* **2015**, *2* (4), 41302. https://doi.org/10.1063/1.4935688.

(3) Laurent, S.; Dutz, S.; Häfeli, U. O.; Mahmoudi, M. Magnetic Fluid Hyperthermia: Focus on Superparamagnetic Iron Oxide Nanoparticles. *Adv. Colloid Interface Sci.* **2011**, *166* (1), 8–23. https://doi.org/10.1016/j.cis.2011.04.003.

(4) Beik, J.; Abed, Z.; Ghoreishi, F. S.; Hosseini-Nami, S.; Mehrzadi, S.; Shakeri-Zadeh, A.; Kamrava, S. K. Nanotechnology in Hyperthermia Cancer Therapy: From Fundamental Principles to Advanced Applications. *J. Control. Release* **2016**, *235*, 205–221. https://doi.org/10.1016/j.jconrel.2016.05.062.

(5) Liu, X.; Zhang, Y.; Wang, Y.; Zhu, W.; Li, G.; Ma, X.; Zhang, Y.; Chen, S.; Tiwari, S.; Shi, K.; Zhang, S.; Fan, H. M.; Zhao, Y. X.; Liang, X.-J. Comprehensive Understanding of Magnetic Hyperthermia for Improving Antitumor Therapeutic Efficacy. *Theranostics* **2020**, *10* (8), 3793–3815. https://doi.org/10.7150/thno.40805.

(6) Srinivasan, S. Y.; Paknikar, K. M.; Bodas, D.; Gajbhiye, V. Applications of Cobalt Ferrite Nanoparticles in Biomedical Nanotechnology. *Nanomedicine* **2018**, *13* (10), 1221–1238. https://doi.org/10.2217/nnm-2017-0379.

(7) Kefeni, K. K.; Msagati, T. A. M.; Nkambule, T. T. I.; Mamba, B. B. Spinel Ferrite Nanoparticles and Nanocomposites for Biomedical Applications and Their Toxicity. *Mater. Sci. Eng. C* **2020**, *107*, 110314. https://doi.org/10.1016/j.msec.2019.110314.

(8) Li, Y.; Huang, G.; Zhang, X.; Li, B.; Chen, Y.; Lu, T.; Lu, T. J.; Xu, F. Magnetic Hydrogels and Their Potential Biomedical Applications. *Adv. Funct. Mater.* **2013**, *23* (6), 660–672.

https://doi.org/10.1002/adfm.201201708.

(9) Veloso, S. R. S.; Ferreira, P. M. T.; Martins, J. A.; Coutinho, P. J. G.; Castanheira, E. M. S. Magnetogels: Prospects and Main Challenges in Biomedical Applications. *Pharmaceutics* **2018**, *10* (3). https://doi.org/10.3390/pharmaceutics10030145.

(10) Campbell, S. B.; Hoare, T. Externally Addressable Hydrogel Nanocomposites for Biomedical Applications. *Curr. Opin. Chem. Eng.* **2014**, *4*, 1–10. https://doi.org/10.1016/j.coche.2013.12.003.

(11) Dahmouche, K.; Santilli, C. V.; Pulcinelli, S. H.; Craievich, A. F. Small-Angle X-Ray Scattering Study of Sol−Gel-Derived Siloxane−PEG and Siloxane−PPG Hybrid Materials. *J. Phys. Chem. B* **1999**, *103* (24), 4937–4942. https://doi.org/10.1021/jp984605h.

(12) Santilli, C. V; Chiavacci, L. A.; Lopes, L.; Pulcinelli, S. H.; Oliveira, A. G. Controlled Drug Release from Ureasil−Polyether Hybrid Materials. *Chem. Mater.* **2009**, *21* (3), 463–467. https://doi.org/10.1021/cm801899u.

(13) Oshiro Junior, A. J.; Paiva Abuçafy, M.; Berbel Manaia, E.; Lallo da Silva, B.; Chiari-Andréo, G. B.; Aparecida Chiavacci, L. Drug Delivery Systems Obtained from Silica Based Organic-Inorganic Hybrids. *Polymers (Basel).* **2016**, *8* (4). https://doi.org/10.3390/polym8040091.

(14) Caravieri, B. B.; de Jesus, N. A. M.; de Oliveira, L. K.; Araujo, M. D.; Andrade, G. P.; Molina, E. F. Ureasil Organic–Inorganic Hybrid as a Potential Carrier for Combined Delivery of Anti-Inflammatory and Anticancer Drugs. *ACS Appl. Bio Mater.* **2019**, *2* (5), 1875–1883. https://doi.org/10.1021/acsabm.8b00798.

(15) Caravieri, B. B.; de Oliveira, P. F.; Furtado, R. A.; Tavares, D. C.; Nassar, E. J.; Ciuffi, K. J.; Molina, E. F. Solubility Enhancement of Ibuprofen Using Tri-Ureasil-PPO Hybrid: Structural, Cytotoxic, and Drug Release Investigation. *J. Sol-Gel Sci. Technol.* **2014**, *72* (3), 627–636. https://doi.org/10.1007/s10971-014-3485-3.

(16) Truffault, L.; Rodrigues, D. F.; Salgado, H. R. N.; Santilli, C. V.; Pulcinelli, S. H. Loaded Ce-Ag Organic-Inorganic Hybrids and Their Antibacterial Activity. *Colloids Surfaces B Biointerfaces* **2016**, *147*, 151–160. https://doi.org/10.1016/j.colsurfb.2016.07.061.

(17) Oshiro Junior, J. A.; Carvalho, F. C.; Soares, C. P.; Chorilli, M.; Chiavacci, L. A. Development of Cutaneous Bioadhesive Ureasil-Polyether Hybrid Films. *Int. J. Polym. Sci.* **2015**, *2015*. https://doi.org/10.1155/2015/727324.

(18) de Jesus, N. A. M.; de Oliveira, A. H. P.; Tavares, D. C.; Furtado, R. A.; de Silva, M. L. A.; Cunha, W. R.; Molina, E. F. Biofilm Formed from a Tri-Ureasil Organic−inorganic Hybrid Gel for Use as a Cubebin Release System. *J. Sol-Gel Sci. Technol.* **2018**, *88* (1), 192–201. https://doi.org/10.1007/s10971-018-4780-1.

(19) Souza, L. K.; Bruno, C. H.; Lopes, L.; Pulcinelli, S. H.; Santilli, C. V; Chiavacci, L. A. Ureasil–Polyether Hybrid Film-Forming Materials. *Colloids Surfaces B Biointerfaces* **2013**, *101*, 156–161. https://doi.org/10.1016/j.colsurfb.2012.06.009.

(20) Molina, E. F.; Pulcinelli, S. H.; Briois, V.; Santilli, C. V. Fine-Tuning of a Nanostructure, Swelling, and Drug Delivery Profile by Blending Ureasil-PEO and Ureasil-PPO Hybrids. *Polym. Chem.* **2014**, *5* (6), 1897–1904. https://doi.org/10.1039/C3PY01126G.

(21) Jesus, C. R. N.; Molina, E. F.; Pulcinelli, S. H.; Santilli, C. V. Highly Controlled Diffusion

Drug Release from Ureasil–Poly(Ethylene Oxide)–Na+–Montmorillonite Hybrid Hydrogel Nanocomposites. *ACS Appl. Mater. Interfaces* **2018**, *10* (22), 19059–19068. https://doi.org/10.1021/acsami.8b04559.

(22) Molina, E. F.; Jesus, C. R. N.; Chiavacci, L. A.; Pulcinelli, S. H.; Briois, V.; Santilli, C. V. Ureasil–Polyether Hybrid Blend with Tuneable Hydrophilic/Hydrophobic Features Based on U-PEO1900 and U-PPO400 Mixtures. *J. Sol-Gel Sci. Technol.* **2014**, *70* (2), 317–328. https://doi.org/10.1007/s10971-014-3300-1.

(23) Caetano, B. L.; Guibert, C.; Fini, R.; Fresnais, J.; Pulcinelli, S. H.; Menager, C.; Santilli, C. V. Magnetic Hyperthermia-Induced Drug Release from Ureasil-PEO-[y]-Fe2O3 Nanocomposites. *RSC Adv.* **2016**, *6* (68), 63291–63295. https://doi.org/10.1039/C6RA08127D.

(24) Ge, J.; Zhai, M.; Zhang, Y.; Bian, J.; Wu, J. Biocompatible Fe3O4/Chitosan Scaffolds with High Magnetism. *Int. J. Biol. Macromol.* **2019**, *128*, 406–413. https://doi.org/10.1016/j.ijbiomac.2019.01.077.

(25) Dhar, P.; Kumar, A.; Katiyar, V. Magnetic Cellulose Nanocrystal Based Anisotropic Polylactic Acid Nanocomposite Films: Influence on Electrical, Magnetic, Thermal, and Mechanical Properties. *ACS Appl. Mater. Interfaces* **2016**, *8* (28), 18393–18409. https://doi.org/10.1021/acsami.6b02828.

(26) Savva, I.; Odysseos, A. D.; Evaggelou, L.; Marinica, O.; Vasile, E.; Vekas, L.; Sarigiannis, Y.; Krasia-Christoforou, T. Fabrication, Characterization, and Evaluation in Drug Release Properties of Magnetoactive Poly(Ethylene Oxide)–Poly(l-Lactide) Electrospun Membranes. *Biomacromolecules* **2013**, *14* (12), 4436–4446.

https://doi.org/10.1021/bm401363v.

(27) Tourinho, F.; Franck, R.; Massart, R.; Perzynski, R. Synthesis and Mangeitc Properties of Managanese and Cobalt Ferrite Ferrite Ferrofluids. In *Trends in Colloid and Interface Science III*; Bothorel, P., Dufourc, E. J., Eds.; Steinkopff: Darmstadt, 1989; pp 128–134.

(28) Dahmouche, K.; Santilli, C. V; Da Silva, M.; Ribeiro, C. A.; Pulcinelli, S. H.; Craievich, A. F. Silica–PEG Hybrid Ormolytes: Structure and Properties. *J. Non. Cryst. Solids* **1999**, *247* (1), 108–113. https://doi.org/10.1016/S0022-3093(99)00042-3.

(29) Schneider, C. A.; Rasband, W. S.; Eliceiri, K. W. NIH Image to ImageJ: 25 Years of Image Analysis. *Nat Meth* **2012**, *9* (7), 671–675. https://doi.org/10.1038/nmeth.2089.

(30) Cryosystems, O. Crystallographica Search-Match. *J. Appl. Crystallogr.* **1999**, *32*, 379–380. https://doi.org/10.1107/S0021889899004124.

(31) Schick, C. Differential Scanning Calorimetry (DSC) of Semicrystalline Polymers. *Anal. Bioanal. Chem.* **2009**, *395* (6), 1589. https://doi.org/10.1007/s00216-009-3169-y.

(32) Foner, S. Versatile and Sensitive Vibrating-Sample Magnetometer. *Rev. Sci. Instrum.* **1959**, *30* (7), 548–557. https://doi.org/10.1063/1.1716679.

(33) Howe, J. M. Bonding, Structure, and Properties of Metal/Ceramic Interfaces: Part 1 Chemical Bonding, Chemical Reaction, and Interfacial Structure. *Int. Mater. Rev.* **1993**, *38* (5), 233–256. https://doi.org/10.1179/imr.1993.38.5.233.

(34) Obeid, L.; Bée, A.; Talbot, D.; Jaafar, S. Ben; Dupuis, V.; Abramson, S.; Cabuil, V.; Welschbillig, M. Chitosan/Maghemite Composite: A Magsorbent for the Adsorption of Methyl Orange. *J. Colloid Interface Sci.* **2013**, *410*, 52–58.

https://doi.org/https://doi.org/10.1016/j.jcis.2013.07.057.

(35) Mohamed, R. M.; Rashad, M. M.; Haraz, F. A.; Sigmund, W. Structure and Magnetic Properties of Nanocrystalline Cobalt Ferrite Powders Synthesized Using Organic Acid Precursor Method. *J. Magn. Magn. Mater.* **2010**, *322* (14), 2058–2064. https://doi.org/10.1016/j.jmmm.2010.01.034.

(36) Li, T.; Senesi, A. J.; Lee, B. Small Angle X-Ray Scattering for Nanoparticle Research. *Chem. Rev.* **2016**, *116* (18), 11128–11180. https://doi.org/10.1021/acs.chemrev.5b00690.

(37) Craievich, A. F. Small-Angle X-Ray Scattering by Nanostructured Materials. In *Handbook of Sol-Gel Science and Technology: Processing, Characterization and Applications*; Klein, L., Aparicio, M., Jitianu, A., Eds.; Springer International Publishing: Cham, 2018; pp 1185–1230. https://doi.org/10.1007/978-3-319-32101-1_37.

(38) Guibert, C.; Dupuis, V.; Peyre, V.; Fresnais, J. Hyperthermia of Magnetic Nanoparticles: Experimental Study of the Role of Aggregation. *J. Phys. Chem. C* **2015**, *119* (50), 28148–28154. https://doi.org/10.1021/acs.jpcc.5b07796.

(39) de Zea Bermudez, V.; Sá Ferreira, R. A.; Carlos, L. D.; Molina, C.; Dahmouche, K.; Ribeiro, S. J. L. Coordination of Eu3+ Ions in Siliceous Nanohybrids Containing Short Polyether Chains and Bridging Urea Cross-Links. *J. Phys. Chem. B* **2001**, *105* (17), 3378–3386. https://doi.org/10.1021/jp002665t.

(40) de Zea Bermudez, V.; Carlos, L. D.; Alcácer, L. Sol−Gel Derived Urea Cross-Linked Organically Modified Silicates. 1. Room Temperature Mid-Infrared Spectra. *Chem. Mater.* **1999**, *11* (3), 569–580. https://doi.org/10.1021/cm980372v.

(41) Gonçalves, M. C.; de Zea Bermudez, V.; Ostrovskii, D.; Carlos, L. D. Cationic and Anionic Environments in Mono-Urethanesil Hybrids Doped with Magnesium Triflate. *Solid State Ionics* **2004**, *166* (1), 103–114. https://doi.org/10.1016/j.ssi.2003.11.003.

(42) Lopes, L.; Molina, E. F.; Chiavacci, L. A.; Santilli, C. V; Briois, V.; Pulcinelli, S. H. Drug–Matrix Interaction of Sodium Diclofenac Incorporated into Ureasil–Poly(Ethylene Oxide) Hybrid Materials. *RSC Adv.* **2012**, *2* (13), 5629–5636. https://doi.org/10.1039/C2RA01216B.

(43) Chung, D. D. L. Thermal Properties. In *Composite Materials: Science and Applications*; Springer London: London, 2010; pp 277–331. https://doi.org/10.1007/978-1-84882-831-5_8.

(44) Mya, K. Y.; Pramoda, K. P.; He, C. B. Crystallization Behavior of Star-Shaped Poly(Ethylene Oxide) with Cubic Silsesquioxane (CSSQ) Core. *Polymer (Guildf).* **2006**, *47* (14), 5035–5043. https://doi.org/10.1016/j.polymer.2006.04.068.

(45) Strawhecker, K. E.; Manias, E. Crystallization Behavior of Poly(Ethylene Oxide) in the Presence of Na+ Montmorillonite Fillers. *Chem. Mater.* **2003**, *15* (4), 844–849. https://doi.org/10.1021/cm0212865.

(46) Palácio, G.; Pulcinelli, S. H.; Mahiou, R.; Boyer, D.; Chadeyron, G.; Santilli, C. V. Coupling Photoluminescence and Ionic Conduction Properties Using the Different Coordination Sites of Ureasil–Polyether Hybrid Materials. *ACS Appl. Mater. Interfaces* **2018**, *10* (43), 37364–37373. https://doi.org/10.1021/acsami.8b11149.

(47) Sadeghi-Avalshahr, A.; Khorsand-Ghayeni, M.; Nokhasteh, S.; Mahdavi Shahri, M.;

Molavi, A. M.; Sadeghi-Avalshahr, M. Effects of Hydroxyapatite (HA) Particles on the PLLA Polymeric Matrix for Fabrication of Absorbable Interference Screws. *Polym. Bull.* **2018**, *75* (6), 2559–2574. https://doi.org/10.1007/s00289-017-2158-0.

(48) Mathen, J. J.; Madhavan, J.; Thomas, A.; Edakkara, A. J.; Sebastian, J.; Joseph, G. P. Transparent ZnO–PVA Binary Composite for UV-A Photo Detector: Optical, Electrical and Thermal Properties Followed by Laser Induced Fluorescence. *J. Mater. Sci. Mater. Electron.* **2017**, *28* (10), 7190–7203. https://doi.org/10.1007/s10854-017-6400-1.

(49) Ash, B. J.; Siegel, R. W.; Schadler, L. S. Glass-Transition Temperature Behavior of Alumina/PMMA Nanocomposites. *J. Polym. Sci. Part B Polym. Phys.* **2004**, *42* (23), 4371–4383. https://doi.org/https://doi.org/10.1002/polb.20297.

(50) Bailey, E. J.; Winey, K. I. Dynamics of Polymer Segments, Polymer Chains, and Nanoparticles in Polymer Nanocomposite Melts: A Review. *Prog. Polym. Sci.* **2020**, *105*, 101242. https://doi.org/10.1016/j.progpolymsci.2020.101242.

(51) Lin, C.-C.; Parrish, E.; Composto, R. J. Macromolecule and Particle Dynamics in Confined Media. *Macromolecules* **2016**, *49* (16), 5755–5772. https://doi.org/10.1021/acs.macromol.6b00471.

(52) Fetters, L. J.; Lohse, D. J.; Colby, R. H. Chain Dimensions and Entanglement Spacings. In *Physical Properties of Polymers Handbook*; Mark, J. E., Ed.; Springer New York: New York, NY, 2007; pp 447–454. https://doi.org/10.1007/978-0-387-69002-5_25.

(53) Binnewies, M.; Milke, E. Data Section C. In *Thermochemical Data of Elements and Compounds*; Wiley Online Books; 2002; pp 229–450.

https://doi.org/10.1002/9783527618347.ch5c.

(54) Krishnan, K. M. Biomedical Nanomagnetics: A Spin Through Possibilities in Imaging, Diagnostics, and Therapy. *IEEE Trans. Magn.* **2010**, *46* (7), 2523–2558. https://doi.org/10.1109/TMAG.2010.2046907.

(55) Karaagac, O.; Yildiz, B. B.; Köçkar, H. The Influence of Synthesis Parameters on One-Step Synthesized Superparamagnetic Cobalt Ferrite Nanoparticles with High Saturation Magnetization. *J. Magn. Magn. Mater.* **2019**, *473*, 262–267. https://doi.org/10.1016/j.jmmm.2018.10.063.

(56) Situ, S. F.; Cao, J.; Chen, C.; Abenojar, E. C.; Maia, J. M.; Samia, A. C. S. Reactive Extrusion Strategies to Fabricate Magnetite–Polyethylene Nanocomposites with Enhanced Mechanical and Magnetic Hyperthermia Properties. *Macromol. Mater. Eng.* **2016**, *301* (12), 1525–1536. https://doi.org/10.1002/mame.201600249.

(57) Abenojar, E. C.; Wickramasinghe, S.; Bas-Concepcion, J.; Samia, A. C. S. Structural Effects on the Magnetic Hyperthermia Properties of Iron Oxide Nanoparticles. *Prog. Nat. Sci. Mater. Int.* **2016**, *26* (5), 440–448. https://doi.org/10.1016/j.pnsc.2016.09.004.

(58) Abramson, S.; Dupuis, V.; Neveu, S.; Beaunier, P.; Montero, D. Preparation of Highly Anisotropic Cobalt Ferrite/Silica Microellipsoids Using an External Magnetic Field. *Langmuir* **2014**, *30* (30), 9190–9200. https://doi.org/10.1021/la501547q.

(59) Wildeboer, R. R.; Southern, P.; Pankhurst, Q. A. On the Reliable Measurement of Specific Absorption Rates and Intrinsic Loss Parameters in Magnetic Hyperthermia Materials. *J. Phys. D. Appl. Phys.* **2014**, *47* (49), 495003. https://doi.org/10.1088/0022-

3727/47/49/495003.

(60) Lanier, O. L.; Korotych, O. I.; Monsalve, A. G.; Wable, D.; Savliwala, S.; Grooms, N. W. F.; Nacea, C.; Tuitt, O. R.; Dobson, J. Evaluation of Magnetic Nanoparticles for Magnetic Fluid Hyperthermia. *Int. J. Hyperth.* **2019**, *36* (1), 686–700. https://doi.org/10.1080/02656736.2019.1628313.

(61) Engelmann, U. M.; Seifert, J.; Mues, B.; Roitsch, S.; Ménager, C.; Schmidt, A. M.; Slabu, I. Heating Efficiency of Magnetic Nanoparticles Decreases with Gradual Immobilization in Hydrogels. *J. Magn. Magn. Mater.* **2019**, *471*, 486–494. https://doi.org/10.1016/j.jmmm.2018.09.113.

(62) Paredes Zaldivar, M.; Santilli, C. V.; Peniche Covas, C. A.; Pulcinelli, S. H. Thermal Properties, Nanoscopic Structure and Swelling Behavior of Chitosan/(Ureasil–Polyethylene Oxide Hybrid) Blends. *J. Therm. Anal. Calorim.* **2017**, *130* (2), 791–798. https://doi.org/10.1007/s10973-017-6454-6.

(63) Korsmeyer, R. W.; Gurny, R.; Doelker, E.; Buri, P.; Peppas, N. A. Mechanisms of Solute Release from Porous Hydrophilic Polymers. *Int. J. Pharm.* **1983**, *15* (1), 25–35. https://doi.org/10.1016/0378-5173(83)90064-9.